Spin rectification for collinear and noncollinear magnetization and external magnetic field configurations

Y. Huo,[1,2,*] L. H. Bai,[2] P. Hyde,[2] Y. Z. Wu,[1] and C.-M. Hu[2]

[1]*Department of Physics, State Key Laboratory of Surface Physics and Collaborative Innovation Center of Advanced Microstructures, Fudan University, Shanghai 200433, China*

[2]*Department of Physics and Astronomy, University of Manitoba, Winnipeg, Manitoba, Canada R3T 2N2*

(Received 23 February 2015; revised manuscript received 27 April 2015; published 26 May 2015)

Spin rectification in a single crystal Fe/Au/Fe sandwich is electrically detected for collinear and noncollinear magnetization and external magnetic field configurations. The line shape, linewidth, and signal polarity are analyzed. The spin rectification theory has been much extended by taking the magnetocrystalline anisotropy and shape anisotropy into account, which explains noncollinear resonances and agrees very well with experimental data. Thus, a comprehensive understanding of spin rectification in ferromagnetic metal is demonstrated in this work.

DOI: 10.1103/PhysRevB.91.174430 PACS number(s): 67.30.hj, 76.50.+g, 75.30.Gw, 75.47.−m

I. INTRODUCTION

A decade ago, spin dynamics in ferromagnetic materials was electrically detected via the spin diode effect in magnetotunnel junctions [1,2] and the bolometric effect in thin films [3,4], which triggered a rapid development. Later, more methods were developed, such as the spin pumping effect [5], the (inverse) spin Hall effect [6], and the spin rectification effect (SRE) [7–23]. As detailed in two recent review articles of spin rectification [24,25], the SRE dominates the electrical voltage induced by ferromagnetic resonance (FMR) in a variety of ferromagnetic metals. A precessing magnetization leads to a periodically changing resistance through magnetoresistance. SRE occurs when a periodically changing resistance couples with the microwave current flowing inside and generates a dc voltage [10]. This became the most popular method in the electrical detection of FMR because of its high sensitivity, simple sample structure, and experimental setup. It was applied to different materials and structures with accurate agreement between theory and experimental results on both the line shape and linewidth [24,25]. Such a line shape analysis is useful for distinguishing spin rectification from spin pumping and the inverse spin Hall effect [13,20,21]. The linewidth is also important for determining additional damping due to spin pumping as well as the intrinsic Gilbert damping [10,26,27]. Almost all the previous studies of the line shape and linewidth were performed in a collinear case where the magnetization is aligned parallel with the external magnetic field. However, in ferromagnetic thin films, the magnetization orientates along an effective field direction rather than the external magnetic field direction, especially when the internal magnetic fields, such as the magnetic anisotropy field and demagnetization field, are comparable to the external magnetic field. In such a noncollinear case of magnetization and external magnetic field, line shape and linewidth analyses of spin rectification have yet to be systematically studied.

In this paper, we experimentally study the line shape and linewidth of spin rectification in a noncollinear case for a sample with strong anisotropy. We also extend spin rectification theory from the collinear case into the noncollinear case by considering all anisotropy effects. Thus, we present a comprehensive understanding of spin rectification in a metallic system.

II. EXPERIMENT

To achieve a system with strong anisotropy, we designed an ultrathin single crystal Fe/Au/Fe sandwich on a MgO (001) substrate by using molecular beam epitaxy in an ultrahigh vacuum chamber. The substrate was cleaned by annealing at 680 °C for 45 min. Then, a 7-nm-thick Fe layer was prepared at room temperature and annealed at 250 °C for 3 min until a high crystalline quality was achieved, as indicated by a sharp reflection of the high-energy electron diffraction (RHEED) pattern, as shown in Fig. 1(a). A 4-nm-thick Au layer was then epitaxially deposited at room temperature. A 3-nm-thick Fe layer was then epitaxially deposited. Further, a 5-nm-thick MgO layer was deposited on top for protection. The RHEED patterns shown in Figs. 1(a)–1(c) indicate the smoothness of each layer surface and the high crystalline quality of the sample. In addition to the shape anisotropy, the single crystal Fe ultrathin film on MgO (001) has a strong in-plane magnetocrystalline anisotropy with the easy axis along the Fe [100] and the hard axis along Fe [110] [28], and the two Fe layers with different thicknesses will have different magnetic anisotropies [29,30], which have all been confirmed by our measurements. Both the magnetocrystalline anisotropy and shape anisotropy in the Fe/Au/Fe sandwich allow us to study noncollinear spin rectification.

As shown in Fig. 1(d), the trilayer sample was patterned into a strip along the Fe [100] easy axis with the dimensions of 20 μm × 3 mm using standard photolithography. A microwave was applied directly into the strip, and most microwave current flows inside of the Au layer due to its high conductivity. Thus, the microwave magnetic field on the bottom layer has a phase shift of π with that in the top layer. The microwave was modulated with a frequency of 8.33 kHz. Voltage was measured along the strip using a lock-in technique. An external magnetic field **H** was applied to the strip with the orientation defined in Fig. 1(d). Spin rectification voltage was measured by sweeping the external magnetic field at a fixed microwave frequency. In this work, the microwave power is 100 mW. Before taking systematic measurements, we have checked

*11110190012@fudan.edu.cn

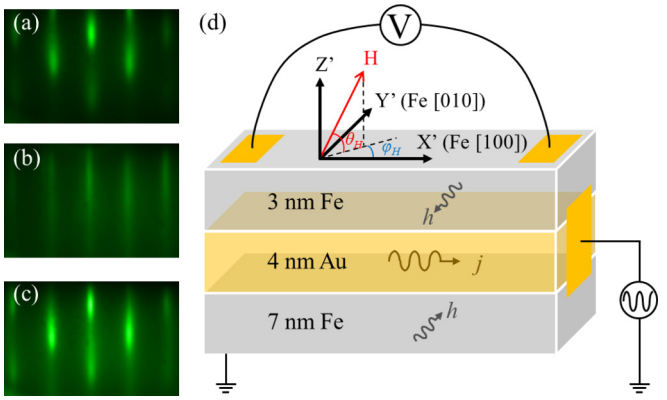

FIG. 1. (Color online) RHEED patterns with the electron beam e^- along MgO ⟨100⟩ of (a) Fe (7 nm)/MgO, (b) Au (4 nm)/Fe (7 nm)/MgO, and (c) Fe (3 nm)/Au (4 nm)/Fe (7 nm)/MgO. (d) Sketch of the measurement geometry.

the magnetization coupling and the spin dynamic coupling between the two Fe layers. When FMR occurs in both Fe layers in our sample, we observed a simple crossing in the ω-H dispersion of FMR for 3 and 7 nm Fe. Usually, the magnetic coupling between two FM layers can induce an anticrossing in the ω-H dispersion [31–34], so the lack of anticrossing in our measurement indicates that magnetic coupling can be ignored in our sample. Moreover, around the crossing, no significant linewidth reduction [35] or amplitude enhancement [22] of the resonance peaks are observed, and then the spin dynamic coupling can be considered to be too weak to influence the FMR of both Fe layers. Thus, we can consider the two Fe layers as two independent FM layers without magnetic coupling and spin dynamic coupling. We have carefully checked the sample at the special geometry [20] for measuring the pure spin pumping signal, which is negligibly small compared to that of spin rectification. Thus, we were allowed to study the line shape, linewidth, and polarity of the pure spin rectification signal in both the collinear and noncollinear cases.

III. RESULTS AND DISCUSSION

Figure 2 shows the results when **H** is applied near the Fe [110] direction in the film plane, which is the hard axis of fourfold magnetocrystalline anisotropy. Figure 2(a) shows a sketch of an in-plane configuration measurement with $\varphi_H \approx 45^\circ$ and $\vartheta_H = 0^\circ$. For this case, when **H** is larger than the saturation field, the magnetization **M** will lie almost parallel to the **H** direction, while if **H** is smaller than the saturation field, **M** will be pulled out of the collinear configuration, and the relative angle between **M** and **H** will be determined by the competition between the Zeeman energy and the fourfold magnetocrystalline anisotropy energy. Figure 2(b) shows an ω-H dispersion plot with the normalized rectification voltage amplitude mapped into a rainbow color scale. The dispersion curves can be calculated by solving the Landau-Lifshitz-Gilbert (LLG) equation [28]. By fitting with the measurement data, we obtained the fourfold magnetic anisotropy field $\mu_0 H_1 = 73$ mT, the effective magnetization $\mu_0 M_{\text{eff}} = 1.7$ T (black solid line), and $\mu_0 H_1 = 26$ mT, $\mu_0 M_{\text{eff}} = 1.4$ T (gray

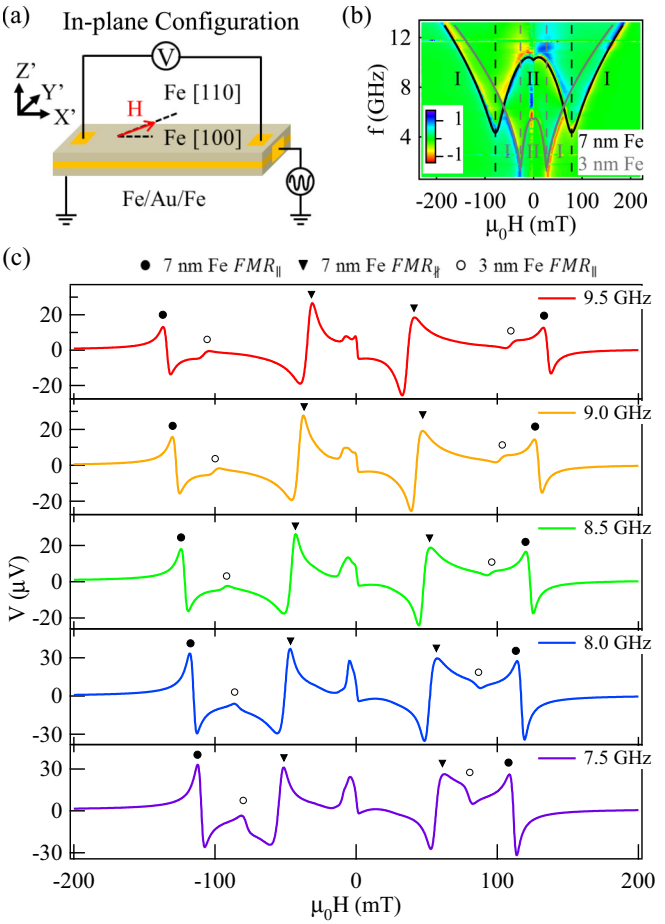

FIG. 2. (Color online) V_{SR} measurement with **H** along the hard axis Fe [110] in plane. (a) Sketch of the in-plane configuration measurement. (b) ω-H dispersion image plot: The gray solid line is the fitting curve of 3 nm Fe, and the black solid line is the fitting curve of 7 nm Fe. Both dispersion curves have two branches: Branch I is the $\text{FMR}_\parallel$ branch, and branch II is the $\text{FMR}_\nparallel$ branch. (c) Typical curves in the in-plane configuration: Solid circles (●) indicate peaks belonging to the $\text{FMR}_\parallel$ branch in 7 nm Fe, solid triangles (▼) indicate peaks belonging to $\text{FMR}_\nparallel$ in 7 nm Fe, and open circles (○) indicate peaks belonging to $\text{FMR}_\parallel$ in 3 nm Fe.

solid line) for two Fe layers. By the Fe thickness dependence of anisotropy in Fe/MgO (001) systems [29,30], we can identify the dispersion curve traced by the black solid line as originating from the 7 nm Fe layer and the curve traced by the gray solid line as originating from the 3 nm Fe layer. These two dispersion curves cross at $\mu_0 H = \pm 65$ mT. The independence of the two dispersion curves near the crossing indicates the coupling between the two FM layers is ignorable for the reasons discussed above. Both the ω-H dispersion curves have two branches, as shown in Fig. 2(b). In branch I, the resonance field increases with the frequency; here, **H** is larger than the saturation field and thus **M** ∥ **H**; we define the resonance in this situation as the $\text{FMR}_\parallel$ branch. In branch II, the resonance field decreases as the frequency increases; here, **H** is smaller than the saturation field and thus **M** ∦ **H**; we define the resonance in this situation as the $\text{FMR}_\nparallel$ branch. Figure 2(c) shows some typical curves measured in

this configuration at various microwave frequencies between 7.5 and 9.5 GHz. At resonance, the SRE curves can be separated into the antisymmetric Lorentzian shape and the Lorentzian shape, but overall the curves are dominated by the antisymmetric Lorentzian line shape, which indicates that the relative phase Φ between the microwave field **h** and microwave current **j** almost has the value of the integer number of π [14]. In addition to the rectification voltage observed at the FMR fields of the 3 nm Fe and 7 nm Fe, a nonresonant rectification signal is observed around $\mu_0 H = 0$, and this signal can be attributed to the spin rotation while the magnetic field reverses, as discussed in Ref. [36]. In this paper we shall focus our study only on the resonance rectification voltage. From Fig. 2(c), we summarize the main features of the SRE measured in the in-plane configuration by Eq. (1): (a) All voltage signals change their polarity when the applied magnetic field reverses; (b) the voltage polarity in the 7 nm Fe $\mathrm{FMR}_{\parallel}$ branch is opposite to the polarity in the 3 nm Fe $\mathrm{FMR}_{\parallel}$ branch; and (c) the voltage polarity in the $\mathrm{FMR}_{\parallel}$ branch is opposite to the polarity in the $\mathrm{FMR}_{\nparallel}$ branch.

At $\varphi_H \approx 45^\circ, \vartheta_H = 0^\circ$,

$$V(H) = -V(-H), \tag{1a}$$

$$\frac{V_{\mathrm{Fe}_7}}{|V_{\mathrm{Fe}_7}|} = -\frac{V_{\mathrm{Fe}_3}}{|V_{\mathrm{Fe}_3}|}, \tag{1b}$$

$$\frac{V_{\mathrm{FMR}_{\parallel}}}{|V_{\mathrm{FMR}_{\parallel}}|} = -\frac{V_{\mathrm{FMR}_{\nparallel}}}{|V_{\mathrm{FMR}_{\nparallel}}|}. \tag{1c}$$

Equation (1a) is in agreement with the studies in the literature [10,14,20], and Eq. (1b) describes the polarity difference in the two Fe layers due to the phase shift of the microwave field. Equation (1c) indicates that in the in-plane configuration the polarity of V_{SR} changes its sign for the case where **M** and **H** are noncollinear. In Fig. 2(c), the resonance peaks in the $\mathrm{FMR}_{\nparallel}$ branch are much broader than those in the $\mathrm{FMR}_{\parallel}$ branch.

In addition to magnetic anisotropy, the shape anisotropy is also able to affect the relative angle between **M** and **H**. Figure 3 shows the results when **H** is applied almost perpendicular to the film plane, with Fig. 3(a) showing a sketch of an out-of-plane measurement configuration with $\varphi_H = 0^\circ$ and $\vartheta_H \approx 90^\circ$. In this configuration, $\mathbf{M} \parallel \mathbf{H}$ for **H** is larger than the saturation field, and $\mathbf{M} \nparallel \mathbf{H}$ for **H** is smaller than the saturation field. The relative angle between **M** and **H** is determined by the competition between the Zeeman energy and shape anisotropy energy. In our system, the effective shape anisotropy field is $\mu_0 M_{\mathrm{eff}} = 1.7$ T for 7 nm Fe and $\mu_0 M_{\mathrm{eff}} = 1.4$ T for 3 nm Fe. Figure 3(b) shows an ω-H dispersion plot, with the normalized rectification voltage amplitude mapped into a rainbow color scale as the indicator marks. We can identify the dispersion curve traced by the black solid line as originating from the 7 nm Fe layer and the curve traced by the gray solid line as originating from the 3 nm Fe layer. Both dispersion curves also have a $\mathrm{FMR}_{\parallel}$ branch and a $\mathrm{FMR}_{\nparallel}$ branch. Figure 3(c) shows several typical curves measured in this configuration at various microwave frequencies between 3.8 and 4.2 GHz. All the resonance peaks are dominated by the Lorentzian line shape, and we describe the key features by Eq. (2).

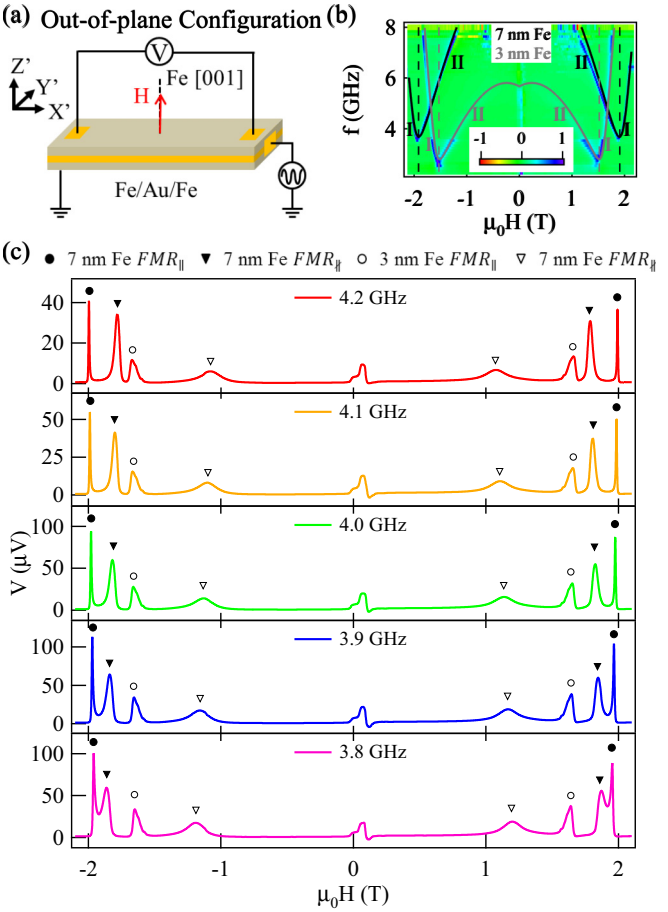

FIG. 3. (Color online) V_{SR} measurement with **H** pointing out of the film plane. (a) Sketch of the out-of-plane configuration measurement. (b) ω-H dispersion image plot: The gray solid line is the fitting curve of 3 nm Fe, and the black solid line is the fitting curve of 7 nm Fe. Both dispersion curves have two branches: Branch I is the $\mathrm{FMR}_{\parallel}$ branch and branch II is the $\mathrm{FMR}_{\nparallel}$ branch. (c) Typical curves in the out-of-plane configuration: Solid circles (●) indicate peaks belonging to the $\mathrm{FMR}_{\parallel}$ branch in 7 nm Fe, solid triangles (▼) indicate peaks belonging to the $\mathrm{FMR}_{\nparallel}$ branch in 7 nm Fe, open circles (○) indicate peaks belonging to the $\mathrm{FMR}_{\parallel}$ branch in 3 nm Fe, and open triangles (▽) indicate peaks belonging to the $\mathrm{FMR}_{\nparallel}$ branch in 3 nm Fe.

At $\varphi_H = 0^\circ, \vartheta_H \approx 90^\circ$,

$$V(H) = V(-H), \tag{2a}$$

$$\frac{V_{\mathrm{Fe}_7}}{|V_{\mathrm{Fe}_7}|} = \frac{V_{\mathrm{Fe}_3}}{|V_{\mathrm{Fe}_3}|}, \tag{2b}$$

$$\frac{V_{\mathrm{FMR}_{\parallel}}}{|V_{\mathrm{FMR}_{\parallel}}|} = \frac{V_{\mathrm{FMR}_{\nparallel}}}{|V_{\mathrm{FMR}_{\nparallel}}|}. \tag{2c}$$

Equation (2) are quite different from Eq. (1). Equation (2a) shows the voltage signal keeps the same polarity when **H** reverses, which indicates that spin pumping and the inverse spin Hall effect are ignorable in our measurement [20]. Equation (2b) shows the signal polarity in the two Fe layers are the same and Eq. (2c) shows the signal polarity in the $\mathrm{FMR}_{\nparallel}$ branch remains the same as in the $\mathrm{FMR}_{\parallel}$ branch. From Fig. 3(c), the resonance peaks in the $\mathrm{FMR}_{\nparallel}$ branch are also

much broader than those in the $FMR_{\parallel}$ branch. Comparing Figs. 2 and 3, the SRE signal in the $FMR_{\nparallel}$ branch has the same behavior as in the $FMR_{\parallel}$ branch when changing the measurement configuration. The signal polarities in the two branches are opposite in the in-plane configuration, but the same in the out-of-plane configuration.

IV. THEORY AND CALCULATION

So far, in the literature, the SRE has been systematically studied only in the configuration with $\mathbf{M} \parallel \mathbf{H}$, and the rectification voltage is described by a formula as a function of $\mathbf{H}$ [10]. Since $\mathbf{M}$ and $\mathbf{H}$ are noncollinear in the $FMR_{\nparallel}$ branch, the conclusions in previous studies are no longer suitable here. However, the $\mathbf{M}$ alignment is always parallel to the effective field $\mathbf{H}_{\text{eff}}$ rather than $\mathbf{H}$. Thus, $\mathbf{H}_{\text{eff}}$ instead of $\mathbf{H}$ should be taken into account, especially in ferromagnetic systems with strong anisotropy. $\mathbf{H}_{\text{eff}}$ could be determined by the free energy F of the system. Considering the single crystal magnetic thin film in our case with Zeeman energy, magnetocrystalline anisotropy, and shape anisotropy, one can get F and $\mathbf{H}_{\text{eff}}$ as follows:

$$F = -\mu_0 M H[\cos\theta_H \cos\theta_M \cos(\varphi_M - \varphi_H) + \sin\theta_H \sin\theta_M] + \frac{1}{2}\mu_0 M_{\text{eff}}^2 \sin^2\theta_M + \frac{1}{4}K_1(\sin^2 2\theta_M + \cos^4\theta_M \sin^2 2\varphi_M), \tag{3a}$$

$$(\mu_0 H_{\text{eff}})^2 = \left(\frac{\omega}{\gamma}\right)^2 = \frac{\mu_0^2}{(\mu_0 M \cos\theta_M)^2}\left[\frac{\partial^2 F}{\partial\theta_M^2}\frac{\partial^2 F}{\partial\varphi_M^2} - \left(\frac{\partial^2 F}{\partial\varphi_M \partial\theta_M}\right)^2\right]\Bigg|_{(\theta_M,\varphi_M)}. \tag{3b}$$

Here, μ_0 is susceptibility in a vacuum, M_{eff} is the effective moment, and K_1 is the fourfold anisotropy constant. φ_M, ϑ_M, φ_H, and ϑ_H are the angles of $\mathbf{M}$ and $\mathbf{H}$, as defined in the insets of Figs. 4(a) and 5(a). In the in-plane configuration, $\vartheta_M = \vartheta_H = 0^\circ$, so the effective field is

$$(\mu_0 H_{\text{eff}})^2 = \left[\mu_0 H\cos(\varphi_H - \varphi_M) + \mu_0 M_{\text{eff}} + \mu_0 H_1 - \tfrac{1}{2}\mu_0 H_1 \sin^2 2\varphi_M\right][\mu_0 H\cos(\varphi_H - \varphi_M) + \mu_0 H_1 \cos 4\varphi_M], \tag{4}$$

and in the out-of-plane configuration, $\vartheta_H = 90^\circ, \varphi_M = \varphi_H = 0^\circ$, so the effective field is

$$(\mu_0 H_{\text{eff}})^2 = [\mu_0 H \sin\theta_M + \mu_0 M_{\text{eff}} \cos 2\theta_M + \mu_0 H_1 \cos 4\theta_M] \times [\mu_0 H \cos\theta_H / \cos\theta_M + \mu_0 H_1 \cos^2\theta_M]. \tag{5}$$

Here the fourfold anisotropy $\mu_0 H_1 = 2K_1/M$. Putting the effective field calculated from Eqs. (4) and (5) together with the microwave field $\mathbf{h}_{X'Y'Z'} = [0, h_{Y'}\cos(\delta)e^{i\omega t}, 0]$ into the LLG equation, we can get the dynamic magnetization $\mathbf{m}$. Here, δ is the phase of $\mathbf{h}$. In our system, we define $\delta = 0$ in the 7 nm Fe and $\delta = \pi$ in the 3 nm Fe. The spin rectification voltage can be calculated by $V_{\text{SR}} = \langle j\Delta R\rangle$, where j is the microwave current in the system, and $\Delta R \propto \text{Re}(m)$ is the resistance variation within the system due to AMR and spin precession. Thus we can derive the SRE in the in-plane configuration,

$$V_{\text{SR}} = A\text{Re}(\chi_L) h_{Y'} \cos(\varphi_M + \delta)\sin(2\varphi_M), \tag{6}$$

and the SRE in the out-of-plane configuration,

$$V_{\text{SR}} = A\text{Re}(\chi_T) h_{Y'} \sin(2\theta_M), \tag{7}$$

with

$$A = -\frac{j_{x'}\Delta R}{2M},$$

$$\text{Re}(\chi_L) = -\frac{\omega_M \omega_{H_{\text{eff}}}\left(\omega_{H_{\text{eff}}}^2 - \omega^2\right)}{\left(\omega_{H_{\text{eff}}}^2 - \omega^2\right)^2 + 4\omega_{H_{\text{eff}}}^2 \alpha^2 \omega^2},$$

$$\text{Re}(\chi_T) = \frac{2\alpha\omega^2 \omega_M \omega_{H_{\text{eff}}}}{\left(\omega^2{}_{H_{\text{eff}}} - \omega^2\right)^2 + 4\omega_{H_{\text{eff}}}^2 \alpha^2 \omega^2}.$$

Here, $j_{x'}$ is the microwave current amplitude, $\text{Re}(\chi_L)$ and $\text{Re}(\chi_T)$ are respectively the real parts of the diagonal and nondiagonal elements of the dynamic susceptibility tensor, ω is the applied microwave frequency, $\omega_M = \gamma M$, $\omega_{H_{\text{eff}}} = \gamma H_{\text{eff}}$, γ is the gyromagnetic ratio, and α is the damping constant. The experiment data in Figs. 2 and 3 show that the relative phase Φ between $\mathbf{h}$ and $\mathbf{j}$ is almost an integer of π. To simplify the situation, we fix the relative phase Φ as an integer of π in our calculation, so thus only the real part of χ will contribute to the signal voltage, as discussed by Harder *et al.* [14]. As shown in Eqs. (6) and (7), V_{SR} depends on $\mathbf{H}_{\text{eff}}$ instead of $\mathbf{H}$, and cannot be directly calculated by a simple formula. To analyze the SRE, we first get φ_M and ϑ_M as functions of $\mathbf{H}$ by minimizing the system free energy F in Eq. (3a), then calculate $\mathbf{H}_{\text{eff}}$ with Eq. (3b), and finally calculate V_{SR} using Eqs. (6) and (7).

Figure 4 shows a comparison between calculation and experimental results in the in-plane configuration. Figure 4(a) is a typical experimental curve measured at a microwave frequency of 10 GHz, and Fig. 4(b) shows the calculated curve with the microwave frequency fixed at 10 GHz. The effective field $\mathbf{H}_{\text{eff}}$ as a function of $\mathbf{H}$ in the in-plane configuration is shown in Fig. 4(c). In the calculation, we use $\varphi_H = 44.6^\circ$ and $\vartheta_H = 0^\circ$ for the in-plane configuration, $\mu_0 H_1 = 73$ mT, $\mu_0 M_{\text{eff}} = 1.7$ T for 7 nm Fe, and $\mu_0 H_1 = 26$ mT, $\mu_0 M_{\text{eff}} = 1.4$ T for 3 nm Fe. All these parameters are determined from the dispersion curves in Fig. 2(b). We use $\alpha = 0.006$ determined from the experimental linewidth of the resonance, and set $A_{\text{Fe}_7} = 5 \times A_{\text{Fe}_3}$ to best represent the experimental conditions. The calculation results agree well with the experimental results. From Eq. (6), V_{SR} is determined by the real part of the diagonal elements of the dynamic susceptibility tensor $\text{Re}(\chi_L)$ which has an antisymmetric Lorentzian line shape, so V_{SR} has an antisymmetric Lorentzian line shape as shown in Fig. 4(b), in good agreement with the experimental result. Since $V_{\text{SR}} \propto \cos(\varphi_M + \delta)\sin(2\varphi_M)$, and when $\mathbf{H}$ reverses, the

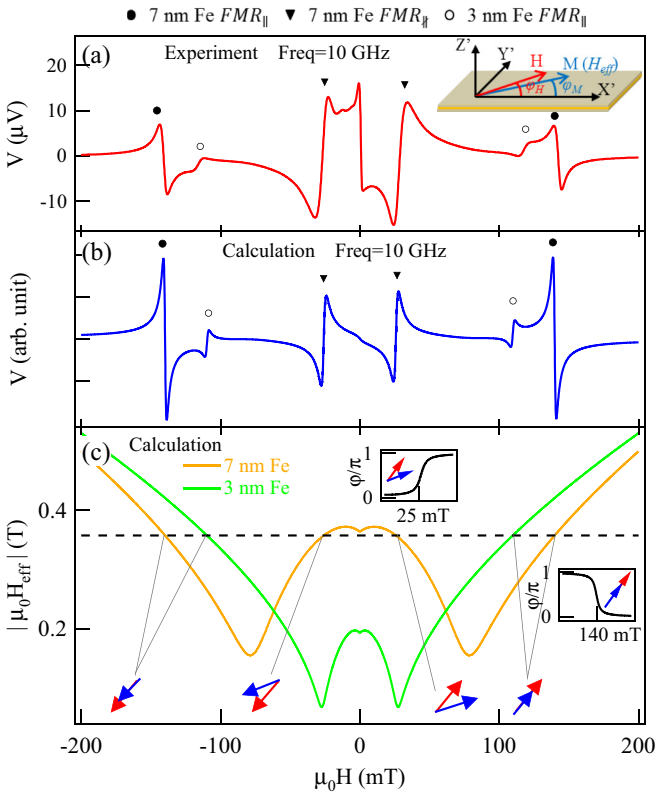

FIG. 4. (Color online) Comparison of experiment and calculation results in the in-plane configuration. (a) Experiment curve with microwave frequency of 10 GHz: The inset shows a noncollinear configuration of **M** and **H** in the in-plane configuration. (b) Calculation curve with microwave frequency fixed at 10 GHz: The result agrees with Eq. (1). Solid lines in (c) are the calculated effective field as a function of the applied field of the 7 nm Fe layer and 3 nm Fe layer in the in-plane configuration, and the dashed line indicates the position of the effective field which satisfies resonance conditions at a microwave frequency of 10 GHz. The insets are the calculated spin resonance phase φ in the $FMR_{\parallel}$ and the $FMR_{\nparallel}$ branches in 7 nm Fe.

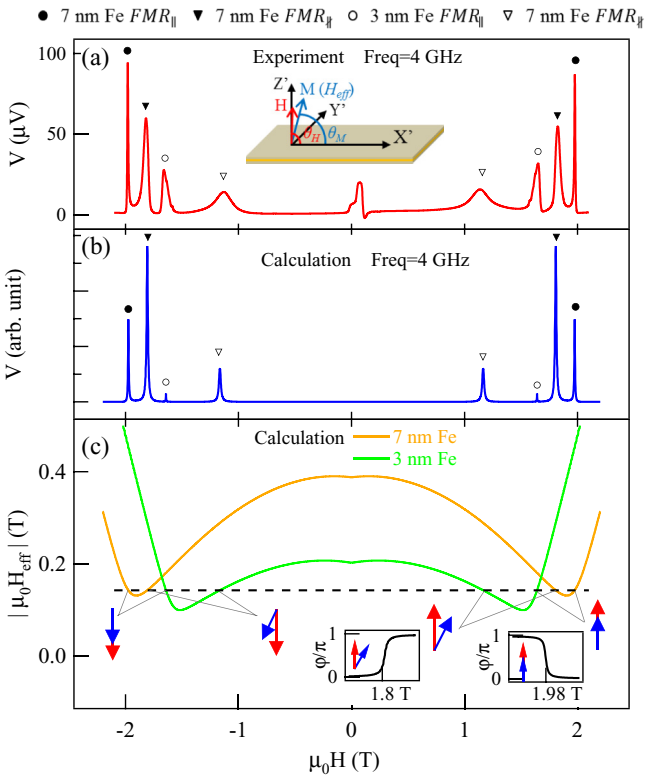

FIG. 5. (Color online) Comparison of experiment and calculation results in the out-of-plane configuration. (a) Experiment curve with a microwave frequency of 4 GHz: The inset shows a noncollinear configuration of **M** and **H** in the out-of-plane configuration. (b) Calculation curve with the microwave frequency fixed at 4 GHz: The result agrees with Eq. (2). Solid lines in (c) are the calculated effective field as a function of the applied field of the 7 nm Fe layer and 3 nm Fe layer in the out-of-plane configuration, and the dashed line indicates the position of the effective field which satisfies resonance conditions at a microwave frequency of 4 GHz. The insets are the calculated spin resonance phase φ in the $FMR_{\parallel}$ and the $FMR_{\nparallel}$ branches in 7 nm Fe.

$\mathbf{H}_{\rm eff}$ and $\mathbf{M}$ will reverse, which corresponds to $\varphi_M + \pi$ and $\vartheta_M + \pi$, and $V_{\rm SR}$ will change its polarity when $\mathbf{H}$ reverses, as shown in Fig. 4(b) and agreeing with Eq. (1a). $V_{\rm SR}$ has the opposite polarity in the 7 nm Fe layer and the 3 nm Fe layer, as shown in Fig. 4(b) and agrees with Eq. (1b), because the phase δ of the rf field $\mathbf{h}$ in these two Fe layers has a difference of π. Near the resonance field, as indicated by the dashed line in Fig. 4(c), $(H - H_0)/(H_{\rm eff} - H_0) > 0$ in the $\rm FMR_{\parallel}$ branch, while $(H - H_0)/(H_{\rm eff} - H_0) < 0$ in the $\rm FMR_{\nparallel}$ branch. Here H_0 is the resonance field. Since the sign of $V_{\rm SR}$ is determined by $(\omega^2_{H_{\rm eff}} - \omega^2)$, the $V_{\rm SR}$-H curve has the opposite polarity in the $\rm FMR_{\parallel}$ and the $\rm FMR_{\nparallel}$ branches, in good agreement with the experiment in Fig. 4(b) as well as with Eq. (1c). Thus, the agreement between experiment and calculation in our system verifies that the approximation of the relative phase Φ as an integer of π is reasonable. If the relative phase Φ shifts from an integer of π, the imaginary part of the dynamic susceptibility χ will contribute to the voltage signal and contribute a Lorentz component to the curve, as discussed by Harder *et al.* [14]. Moreover, if the Lorentz component is much larger than the antisymmetric Lorentz component, the overall line shape will be Lorentzian, and the signal polarity will be similar to that in the out-of-plane configuration we will discuss in the following.

In the out-of-plane configuration, our theory also works well. Figure 5 shows a comparison between calculation and experimental results in the out-of-plane configuration. Figure 5(a) is a typical experimental curve measured at a microwave frequency of 4 GHz, and Fig. 5(b) shows the calculated curve with a microwave frequency of 4 GHz. Figure 5(c) shows the calculated effective field $\mathbf{H}_{\rm eff}$ as a function of $\mathbf{H}$. In our calculation, we use $\varphi_H = 0^\circ$ and $\vartheta_H = 89.4^\circ$ for the out-of-plane configuration, and keep the other parameters the same as those used in the in-plane configuration. Equation (7) shows that $V_{\rm SR}$ is determined by the real part of the nondiagonal elements of the dynamic susceptibility tensor $\mathrm{Re}(\chi_T)$ and has a Lorentzian line shape, which can be proved by the calculated curve in Fig. 5(b), and agrees with experimental results. Since $V_{\rm SR} \propto \sin(2\theta_M)$, $V_{\rm SR}$ keeps the same polarity when $\mathbf{H}$ reverses [agrees with Eq. (2a)], and keeps the same polarity in the 7 nm Fe and the 3 nm Fe

TABLE I. The calculation and the experimental results of the SRE in the $\mathbf{M} \parallel \mathbf{H}$ and the $\mathbf{M} \nparallel \mathbf{H}$ configuration in a 7 nm Fe layer with different measurement geometries. The positive polarity of the SRE is defined as $V_{SR}/|V_{SR}| > 0$ when $H < H_0$. The subscript "expt." indicates the result is extracted from the experimental data, and the subscript "calc" indicates the result is extracted from the calculation data.

	Measurement configuration	Line shape	Polarity	$\mu_0 H_0$ (T)	$\mu_0 \Delta H$ (mT)
$\mathbf{M} \parallel \mathbf{H}$	$\varphi_H = 44.6°$, $\vartheta_H = 0°$, $f = 10$ GHz	Anti-Lorentz$_{(expt.)}$	$-_{(expt.)}$	$0.14_{(expt.)}$	$5.3_{(expt.)}$
		Anti-Lorentz$_{(calc)}$	$-_{(calc)}$	$0.14_{(calc)}$	$2.4_{(calc)}$
	$\varphi_H = 0°$, $\vartheta_H = 89.4°$, $f = 4$ GHz	Lorentz$_{(expt.)}$	$+_{(expt.)}$	$1.96_{(expt.)}$	$9.5_{(expt.)}$
		Lorentz$_{(calc)}$	$+_{(calc)}$	$1.97_{(calc)}$	$7.2_{(calc)}$
$\mathbf{M} \nparallel \mathbf{H}$	$\varphi_H = 44.6°$, $\vartheta_H = 0°$, $f = 10$ GHz	Anti-Lorentz$_{(expt.)}$	$+_{(expt.)}$	$0.03_{(expt.)}$	$10.0_{(expt.)}$
		Anti-Lorentz$_{(calc)}$	$+_{(calc)}$	$0.03_{(calc)}$	$3.6_{(calc)}$
	$\varphi_H = 0°$, $\vartheta_H = 89.4°$, $f = 4$ GHz	Lorentz$_{(expt.)}$	$+_{(expt.)}$	$1.79_{(expt.)}$	$54.0_{(expt.)}$
		Lorentz$_{(calc)}$	$+_{(calc)}$	$1.80_{(calc)}$	$13.0_{(calc)}$

layer [agrees with Eq. (2b)]. Equation (7) shows that the sign of V_{SR} is determined by $\omega_{H_{eff}}$, so the V_{SR} polarity remains the same in the FMR$_\parallel$ branch and the FMR$_\nparallel$ branch.

We further calculated the spin resonance phase φ in both in-plane and out-of-plane configurations, and the calculated φ in the 7 nm Fe are shown in insets in Figs. 4(c) and 5(c), respectively. The spin resonance phase φ describes the phase lag between the precessing magnetization and the driving microwave field, and can be determined by $\cos\varphi = \mathrm{Re}(\chi)/|\chi|$ [10,14,37]. The insets in Figs. 4(c) and 5(c) show, in the collinear configuration, $\varphi = \pi$ when $H < H_0$, which is called a driving force out of phase, and $\varphi = 0$ when $H > H_0$, which is called a driving force in phase. φ will change from π to 0 as H increases around FMR and $\varphi = \pi/2$ at FMR. Here we define such a phase jump as a negative phase jump. However, in a noncollinear configuration, $\varphi = 0$ (driving force in phase) when $H < H_0$, and $\varphi = \pi$ (driving force out of phase) when $H > H_0$. φ will change from 0 to π as H increases around FMR and $\varphi = \pi/2$ at FMR. Here we define such a phase jump as a positive phase jump. Considering the effective field as shown in Figs. 4(c) and 5(c) rather than the applied field, in both collinear and noncollinear configurations, the phase φ is π when $H_{\mathrm{eff}} < H_0$, and is 0 when $H_{\mathrm{eff}} > H_0$. Also, φ changes from π to 0 as H_{eff} increases around FMR and $\varphi = \pi/2$ at FMR, which means the phase jump is negative in both collinear and noncollinear configurations by considering the effective field. So in both in-plane and out-of-plane configurations, as H increases, the phase φ between the spin precession and the driving microwave magnetic field decreases in the collinear configuration and increases in the noncollinear configurations at FMR, and the difference is due to the different H-dependence effective field in collinear and noncollinear configurations.

The calculation and the experimental results of the SRE in the 7 nm Fe layer are listed in Table I. Our theory well describes the line shape and polarity of the SRE in the general configuration of **M** and **H**. Also, our calculation qualitatively confirms the broadening of the linewidth ΔH for a noncollinear alignment of **M** and **H**. However, the experimental value of the linewidth is much broader than the calculated results, and the linewidth broadening in the noncollinear configuration in the experiment is also much larger than that in theory. In our theory, the effect of the interface on FMR has not been taken into account, however, it is known that some interfacial effects, such as spin pumping and magnon scattering [10,26,27,38], will enhance the linewidth.

Figure 6 directly compares the linewidth in the collinear and noncollinear configurations. The rectification voltage in the FMR$_\parallel$ branch and the FMR$_\nparallel$ branch are plotted against their resonance field $H - H_0$ in the in-plane configuration, as shown in Fig. 6(a). The full width at half maxima δH of FMR at different microwave frequencies are plotted in Fig. 6(b), which clearly shows the broadening of linewidth in the noncollinear configuration. Besides the in-plane configuration, the linewidth in the out-of-plane configuration is also analyzed, and is shown in Figs. 6(c) and 6(d). The linewidth of nonconllinear resonance is much broader than that of collinear resonance for the out-of-plane configuration. In our theory, the Fe layers are only treated as a single domain, but in the noncollinear configuration, the magnetization is not saturated and might form a multidomain, which may cause inhomogeneous magnetization and lead to additional damping [39]. Nevertheless, this is still an open question for further study.

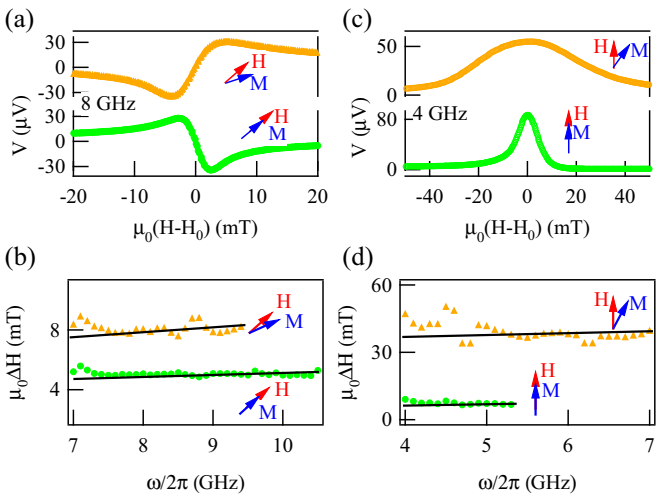

FIG. 6. (Color online) (a) The rectification voltage and (b) the linewidth in the 7 nm Fe in the FMR$_\parallel$ branch and the FMR$_\nparallel$ branch as a function of $H - H_0$ in the in-plane configuration, and (c) the rectification voltage and (d) the linewidth in the out-of-plane configuration. The black lines are guides for the eyes.

V. CONCLUSION

In conclusion, we studied the spin rectification effect in an epitaxial Fe/Au/Fe trilayer system with strong magnetic anisotropy and shape anisotropy. In addition to the SRE when **M** and **H** are collinear, we study V_{SR} for the case where **M** and **H** are noncollinear. The different behaviors of V_{SR} in different configurations of **M** and **H** are due to the relationship between $\mathbf{H}_{eff}$ and **H**. By considering $\mathbf{H}_{eff}$ instead of **H** in ferromagnetic systems, we extend the SRE theory for all **M** and **H** configurations. These equations will help further the understanding of spin transport in ferromagnetic systems, especially for **M** not parallel to **H**.

ACKNOWLEDGMENTS

This project was supported by the National Key Basic Research Program of China (Grants No. 2015CB921401 and No. 2011CB921801), National Science Foundation of China (Grants No. 11274074, No. 11434003, No. 11474066, and No. 11429401) and NSERC grants. The authors thank J. X. Li from Fudan University, Z. H. Zhang, B. M. Yao, L. Fu, and Y. S. Gui from University of Manitoba, and X. L. Fan from Lanzhou University.

[1] A. A. Tulapurkar, Y. Suzuki, A. Fukushima, H. Kubota, H. Maehara, K. Tsunekawa, D. D. Djayaprawira, N. Watanabe, and S. Yuasa, Nature (London) **438**, 339 (2005).
[2] J. C. Sankey, P. M. Braganca, A. G. F. Garcia, I. N. Krivorotov, R. A. Buhrman, and D. C. Ralph, Phys. Rev. Lett. **96**, 227601 (2006).
[3] Y. S. Gui, S. Holland, N. Mecking, and C.-M. Hu, Phys. Rev. Lett. **95**, 056807 (2005).
[4] S. T. Goennenwein, S. W. Schink, A. Brandlmaier, A. Boger, M. Opel, R. Gross, R. S. Keizer, T. M. Klapwijk, A. Gupta, H. Huebl, C. Bihler, and M. S. Brandt, Appl. Phys. Lett. **90**, 162507 (2007).
[5] A. Azevedo, L. H. Vilela Leäo, R. L. Rodriguez-Suarez, A. B. Oliveira, and S. M. Rezend, J. Appl. Phys. **97**, 10C715 (2005).
[6] E. Saitoh, M. Ueda, H. Miyajima, and G. Tatara, Appl. Phys. Lett. **88**, 182509 (2006).
[7] M. V. Costache, S. M. Watts, M. Sladkov, C. H. van der Wal, and B. J. van Wees, Appl. Phys. Lett. **89**, 232115 (2006).
[8] Y. S. Gui, N. Mecking, X. Zhou, G. Williams, and C.-M. Hu, Phys. Rev. Lett. **98**, 107602 (2007).
[9] A. Yamaguchi, H. Miyajima, T. Ono, Y. Suzuki, S. Yuasa, A. Tulapurkar, and Y. Nakatani, Appl. Phys. Lett. **90**, 182507 (2007).
[10] N. Mecking, Y. S. Gui, and C.-M. Hu, Phys. Rev. B **76**, 224430 (2007).
[11] T. Moriyama, R. Cao, X. Fan, G. Xuan, B. K. Nikolić, Y. Tserkovnyak, J. Kolodzey, and J. Q. Xiao, Phys. Rev. Lett. **100**, 067602 (2008).
[12] H. Xiong, A. Wirthmann, Y. S. Gui, Y. Tian, X. F. Jin, Z. H. Chen, S. C. Shen, and C.-M. Hu, Appl. Phys. Lett. **93**, 232502 (2008).
[13] O. Mosendz, J. E. Pearson, F. Y. Fradin, G. E. W. Bauer, S. D. Bader, and A. Hoffmann, Phys. Rev. Lett. **104**, 046601 (2010).
[14] M. Harder, Z. X. Cao, Y. S. Gui, X. L. Fan, and C.-M. Hu, Phys. Rev. B **84**, 054423 (2011).
[15] A. Azevedo, L. H. Vilela-Leão, R. L. Rodríguez-Suárez, A. F. Lacerda Santos, and S. M. Rezende, Phys. Rev. B **83**, 144402 (2011).
[16] Z. Feng, J. Hu, L. Sun, B. You, D. Wu, J. Du, W. Zhang, A. Hu, Y. Yang, D. M. Tang, B. S. Zhang, and H. F. Ding, Phys. Rev. B **85**, 214423 (2012).
[17] L. Chen, F. Matsukura, and H. Ohno, Nat. Commun. **4**, 2055 (2013).
[18] E. Th. Papaioannou, P. Fuhrmann, M. B. Jungfleisch, T. Brächer, P. Pirro, V. Lauer, J. Lösch, and B. Hillebrands, Appl. Phys. Lett. **103**, 162401 (2013).
[19] H. Chen, X. Fan, W. Wang, H. Zhou, Y. S. Gui, C.-M. Hu, and D. Xue, Appl. Phys. Lett. **102**, 202410 (2013).
[20] L. H. Bai, P. Hyde, Y. S. Gui, C.-M. Hu, V. Vlaminck, J. E. Pearson, S. D. Bader, and A. Hoffmann, Phys. Rev. Lett. **111**, 217602 (2013).
[21] M. Obstbaum, M. Härtinger, H. G. Bauer, T. Meier, F. Swientek, C. H. Back, and G. Woltersdorf, Phys. Rev. B **89**, 060407(R) (2014).
[22] P. Hyde, L. H. Bai, D. M. J. Kumar, B. W. Southern, C.-M. Hu, S. Y. Huang, B. F. Miao, and C. L. Chien, Phys. Rev. B **89**, 180404(R) (2014).
[23] J. Kleinlein, B. Ocker, and G. Schmidt, Appl. Phys. Lett. **104**, 153507 (2014).
[24] Y. S. Gui, L. H. Bai, and C.-M. Hu, Sci. China: Phys., Mech. Astron. **56**, 124 (2013).
[25] L. H. Bai, Y. S. Gui, and C.-M. Hu, in *Introduction to Spintronics*, edited by X. F. Han *et al.* (Science Press, Beijing, 2014), Chap. 9 (in Chinese).
[26] B. Heinrich, C. Burrowes, E. Montoya, B. Kardasz, E. Girt, Y.-Y. Song, Y. Sun, and M. Wu, Phys. Rev. Lett. **107**, 066604 (2011).
[27] J.-C. Rojas-Sánchez, N. Reyren, P. Laczkowski, W. Savero, J.-P. Attan, C. Deranlot, M. Jamet, J.-M. George, L. Vila, and H. Jaffrès, Phys. Rev. Lett. **112**, 106602 (2014).
[28] G. Counil, J.-V. Kim, T. Devolder, P. Crozat, C. Chappert, and A. Cebollada, J. Appl. Phys. **98**, 023901 (2005).
[29] H. Ohta, S. Imagawa, M. Morokawa, and E. Kita, J. Phys. Soc. Jpn. **62**, 4467 (1993).
[30] G. Chen, J. X. Li, J. Zhu, J. H. Liang, and Y. Z. Wu, J. Appl. Phys. **109**, 07C108 (2011).
[31] P. Grünberg, R. Schreiber, Y. Pang, M. B. Brodsky, and H. Sowers, Phys. Rev. Lett. **57**, 2442 (1986).
[32] A. Layadi and J. O. Artman, J. Magn. Magn. Mater. **92**, 143 (1990).
[33] Y. Chen, X. Fan, Y. Zhou, Y. Xie, J. Wu, T. Wang, S. T. Chui, and J. Q. Xiao, Adv. Mater. **27**, 1351 (2015).

[34] X. M. Liu, Hoa T. Nguyen, J. Ding, M. G. Cottam, and A. O. Adeyeye, Phys. Rev. B **90**, 064428 (2014).
[35] B. Heinrich, Y. Tserkovnyak, G. Woltersdorf, A. Brataas, R. Urban, and G. E. W. Bauer, Phys. Rev. Lett. **90**, 187601 (2003).
[36] X. F. Zhu, M. Harder, J. Tayler, A. Wirthmann, B. Zhang, W. Lu, Y. S. Gui, and C.-M. Hu, Phys. Rev. B **83**, 140402(R) (2011).
[37] A. Wirthmann, X. Fan, Y. S. Gui, K. Martens, G. Williams, J. Dietrich, G. E. Bridges, and C.-M. Hu, Phys. Rev. Lett. **105**, 017202 (2010).
[38] R. Urban, G. Woltersdorf, and B. Heinrich, Phys. Rev. Lett. **87**, 217204 (2001).
[39] S. Zhang and S. S.-L. Zhang, Phys. Rev. Lett. **102**, 086601 (2009).